ACS OMEGA

http://pubs.acs.org/journal/acsodf

Article

Promotion Mechanism of $CaSO_4$ and Au in the Plasma-Assisted Catalytic Oxidation of Diesel Particulate Matter

Chengrong Kong, Shuiliang Yao,* Zuliang Wu, Jing Li, Guojian Li, and Jiali Zhu*

Cite This: *ACS Omega* 2022, 7, 8640−8650

Read Online

ACCESS | Metrics & More | Article Recommendations | Supporting Information

ABSTRACT: Plasma-assisted catalysis has been demonstrated to be an innovative technology for eliminating diesel particulate matter (DPM) efficiently at low temperature (≤200 °C). Moreover, past studies have demonstrated that $CaSO_4$, which exists in small concentrations (<2%) in DPM and is toxic in thermal catalytic oxidation processes, actually enhances DPM oxidation during plasma-assisted catalytic processes. However, the role $CaSO_4$ plays in this promotion of DPM oxidation still remains unclear. The present study addresses this issue by investigating the underlying mechanisms of DPM oxidation during plasma-assisted catalytic processes using graphitic carbon as a surrogate DPM material in conjunction with $CaSO_4$- and Au-impregnated γ-Al_2O_3 catalysts. The results of mass spectrometry and in situ diffuse reflectance infrared Fourier transform spectroscopy, which employs an in situ cell with a small dielectric barrier discharge space over the catalyst bed, demonstrate that $CaSO_4$ can save and release O atoms contributing to graphite oxidation via the −S═O units of $CaSO_4$ through a reversible surface reaction (−S═O + O → $-S(-O)_2$). The results are employed to propose a formal mechanism of graphite oxidation catalyzed by $CaSO_4$ and Au. These findings both improve our understanding of the plasma-assisted catalytic oxidation mechanisms of DPM and support the development of efficient plasma-assisted catalysts.

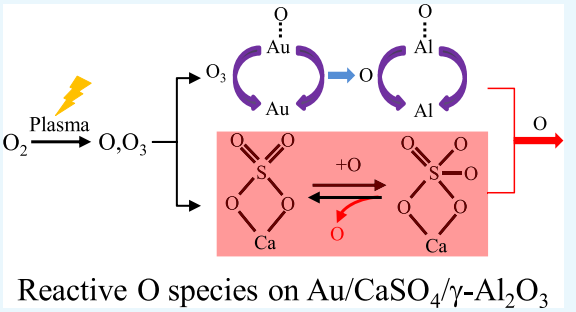

1. INTRODUCTION

Although more and more sustainable vehicles, such as hybrid and electric vehicles, are currently in operation, the carbon neutrality target will not be achieved until around 2060,[1] during which diesel vehicles will still play an irreplaceable role as an important means of transportation due to their good power performance, high energy efficiency, and low CO_2 emissions.[2]

However, these vehicles also emit diesel particulate matter (DPM), which causes serious environmental and health problems.[2] DPM is mainly composed of carbonaceous particles (soot), soluble organic compounds, and inorganic salts (such as $CaSO_4$).[3] As a result, many countries have developed standards limiting DPM emissions, like the Euro VI emission standards[4] and Tier 3 in the United States.[5] Meeting these standards requires the implementation of DPM treatment technologies. The primary treatment that has been developed and commercialized is the diesel particulate filter (DPF) technology.[6−9] While this technology can trap DPM effectively,[10] the accumulation of DPM in the DPF results in a progressively increasing back pressure and reduced diesel engine fuel efficiency. DPF regeneration cannot be completed during low-speed operation, where the exhaust temperature is typically lower than 250 °C. Under these conditions, an active DPF regeneration process must be implemented, which reduces the fuel efficiency of diesel engines.[11] Efforts to address this issue have included the development of catalytic DPF (cDPF) technology, which applies noble catalysts to the interior surfaces of the DPF honeycomb structure to promote DPM oxidation at lower exhaust temperatures (400 °C).[12−14] Nonetheless, existing cDPF technology requires exhaust temperatures higher than 400 °C to function effectively.[15]

Recently, plasma-assisted catalysis technology has been demonstrated to promote DPM oxidation efficiently at low temperatures (≤200 °C).[16−18] For example, Yamamoto et al. compared the DPM oxidation performance obtained by several metal oxide catalysts employed in a dielectric barrier discharge (DBD) plasma reactor at 200 °C and found that Fe_2O_3 provided the best DPM oxidation rate.[19] Sekine et al. found that Ni-impregnated CeO_2 catalysts provided the highest oxidation activity for soot due to the presence of O atoms in the CeO_2 lattice.[20] Similarly, Ranji-Burachaloo et al. reported that the introduction of Co_3O_4 into a DBD plasma reactor increased the DPM removal efficiency from 3.4 to 6.0 g/kW h at 200 °C.[21] Yao et al. evaluated the energy efficiency limitations of the plasma-assisted oxidation removal of DPM

Received: November 24, 2021
Accepted: February 23, 2022
Published: March 7, 2022

and found that this technology can be put into practical use if the energy efficiency can reach a moderate value of 5 g DPM/kW h.[22]

Past studies have demonstrated that the presence of salts such as sulfates significantly improves DPM removal when using metal oxide catalysts in plasma-assisted processes.[23−25] Furuta et al. attributed this promotional effect of sulfates to their electron-absorbing ability, which induces the formation of Lewis acid sites on metal oxides in the catalytic reaction.[26] Yao et al. found that an Au- and $CaSO_4$-impregnated γ-Al_2O_3 catalyst was more effective for plasma-assisted DPM removal than an Au-impregnated γ-Al_2O_3 catalyst. This study also demonstrated that the removal of DPM from the exhaust of a diesel power generator using a DBD reactor with an Au- and $CaSO_4$-impregnated γ-Al_2O_3 catalyst was as high as 91%.[27] In fact, this level is comparable to that of a DPF, indicating that plasma catalysis is practicable for DPM removal. Unfortunately, the mechanism by which sulfates promote DPM oxidation in a plasma-assisted context remains poorly understood.

The effect of sulfates has also been investigated in the thermal oxidation of soot with Pt-impregnated Al_2O_3 catalysts (Pt/Al_2O_3) and sulfate-impregnated Pt/Al_2O_3 catalysts in the presence of NO.[28] Here, the soot oxidation process was observed to be promoted, and the oxygen was then transferred to the surface of soot particles to form surface oxygen compounds (SOCs). Moreover, the presence of sulfate was demonstrated to promote CO_2 formation. Kikugawa et al. investigated the soot oxidation activity and oxidation mechanism of Ag_2SO_4-impregnated Al_2O_3 catalysts in thermal catalytic processes, and higher soot oxidation activity was observed under loose contact conditions compared to Ag-impregnated Al_2O_3.[29]

Efforts to establish the role of sulfates in these catalytic processes can benefit from the role of sulfates established in other types of processes, such as in the selective catalytic reduction of nitric oxide by ammonia and the oxidation of hydrocarbons via thermal catalytic processes.[30] For example, Chen et al. discovered that the presence of sulfate can create new and stronger Lewis acid sites on CeO_2 and Fe_2O_3 particle surfaces and deactivate sources of surface oxygen that can suppress the NH_3 oxidation side reaction.[31] Surely, such a finding presents an exciting opportunity for future catalyst design with high durability and low cost. Zhang et al. demonstrated that SO_4^{2-}-impregnated Fe_2O_3 catalysts present considerable activity for dichloromethane combustion, which was found to be dependent on both super strong acidity and the availability of surface oxygen, and the sulfate promotion mechanism was proposed to function mainly through the formation of organic sulfates.[32]

The present study addresses the poorly understood role sulfates play in the promotion of DPM oxidation in a plasma-assisted context by investigating the underlying mechanisms of DPM oxidation during plasma-assisted catalytic processes using graphitic carbon in conjunction with γ-Al_2O_3 catalyst particles impregnated by $CaSO_4$ alone ($CaSO_4/\gamma$-Al_2O_3), Au alone (Au/γ-Al_2O_3), and both $CaSO_4$ and Au (Au/$CaSO_4/\gamma$-Al_2O_3). Here, $CaSO_4$ is a well-suited sulfate for this study because $CaSO_4$ naturally exists in small concentrations in DPM. Graphite is used as the surrogate DPM material because the microstructure of soot is mainly composed of graphite-like microcrystals.[33] The analysis conducted is based on the results of in situ diffuse reflectance infrared Fourier transform spectroscopy (DRIFTS) and mass spectrometry (MS), which is facilitated by the use of an in situ cell with a small DBD space over the catalyst bed. We propose a formal mechanism of graphite oxidation catalyzed by $CaSO_4$ and Au based on the observation that $CaSO_4$ can save and release O atoms contributing to graphite oxidation. The enhanced understanding of the plasma-assisted catalytic oxidation mechanisms of DPM supports the development of efficient plasma catalysts.

2. RESULTS AND DISCUSSION

2.1. Characterization of the Catalysts. TEM images of representative Au/$CaSO_4/\gamma$-Al_2O_3 catalyst particles are presented in Figure S3. The images demonstrate that the secondary Au particles, denoted by the black regions of the images, were uniformly dispersed over the surface of the primary γ-Al_2O_3 particles, and their diameters ranged from 20 to 50 nm. The energy dispersive spectroscopy (EDS) mappings obtained for the major elements in the Au/$CaSO_4/\gamma$-Al_2O_3 catalyst (Figure S4) indicate that the Au, Ca, and S elements are uniformly distributed in this catalyst.

The acidity of a catalyst plays an important role in catalytic oxidation.[34−36] Therefore, NH_3 temperature-programmed desorption (NH_3-TPD) was applied to measure the surface acidities of the γ-Al_2O_3, Au/γ-Al_2O_3, $CaSO_4/\gamma$-Al_2O_3, and Au/$CaSO_4/\gamma$-Al_2O_3 catalysts. Three peaks were found in the ranges of 100−150, 250−350, and 550−700 °C, which correspond to the ammonia desorption on weak acid, medium strong acid, and strong acid sites, respectively (Figure S5). The total ammonia adsorption of the catalysts decreased in the order of Au/$CaSO_4/\gamma$-Al_2O_3 > $CaSO_4/\gamma$-Al_2O_3 > Au/γ-Al_2O_3 > γ-Al_2O_3, suggesting that the ammonia adsorption was enhanced by Au and $CaSO_4$.

It is well known that the activation of O_2 is very important for the oxidation of soot reaction. Therefore, O_2 temperature-programmed desorption (O_2-TPD) was applied to measure the O_2 desorption on the surface sites of γ-Al_2O_3, Au/γ-Al_2O_3, $CaSO_4/\gamma$-Al_2O_3, and Au/$CaSO_4/\gamma$-Al_2O_3 catalysts. As shown in Figure S6, all catalysts exhibited three desorption peaks between 100 and 700 °C. In general, the adsorbed oxygen changes by the following procedures: $O_2(ad) \rightarrow O-2(ad) \rightarrow O^-(ad) \rightarrow O^{2-}(lattice)$. The peak at a lower temperature (100−250 °C) is assigned to the desorption of chemically adsorbed oxygen molecular O− 2(ad).[37] For $CaSO_4/\gamma$-Al_2O_3 and Au/$CaSO_4/\gamma$-Al_2O_3 catalysts, the chemically adsorbed oxygen molecule is easily desorbed. This may be due to the fact that $CaSO_4$ increases the mobility of surface reactive oxygen species (O− 2), and O− 2 plays an important role in the oxidation of graphite under real reaction condition.[38] Meanwhile, the peaks at 250−450 and 450−700 °C are related to chemically adsorbed oxygen atom O^-(ad) and lattice oxygen O^{2-} (lattice), respectively.[37,39] Compared with γ-Al_2O_3 and $CaSO_4/\gamma$-Al_2O_3, two differences were observed in the Au/γ-Al_2O_3 and Au/$CaSO_4/\gamma$-Al_2O_3 catalysts. One is that the desorption peak corresponding to O− 2(ad) and O^{2-}(lattice) shifted to a lower temperature, and the other is that the peaks corresponding to O^-(ad) and O^{2-}(lattice) were easier to be desorbed. Particularly, it is understandable that Au/$CaSO_4/\gamma$-Al_2O_3 catalyst had excellent activity since the activity correlates very well with the surface-active oxygen species, namely more surface-active oxygen species corresponds to a higher catalyst oxidation activity.[40]

The Au 4f X-ray photoelectron spectroscopy (XPS) spectra of Au/γ-Al_2O_3 and Au/$CaSO_4/\gamma$-Al_2O_3 catalysts (Figure S7a)

https://doi.org/10.1021/acsomega.1c06659
ACS Omega 2022, 7, 8640−8650

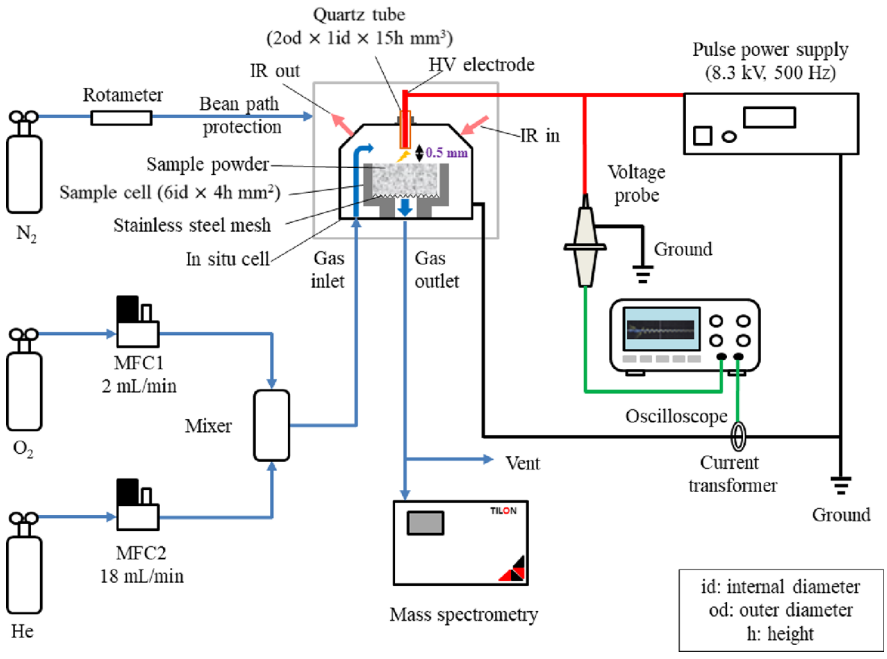

Figure 1. Schematic illustrating the experimental setup of the DBD−DRIFTS−MS system.

indicate the presence of only two Au valence states, which include a state characteristic of metallic gold (Au^0) at an Au $4f_{7/2}$ binding energy of 83.6−84.5 eV, and the Au^{3+} state at an Au $4f_{5/2}$ binding energy of 89.4−90.4 eV and an Au $4f_{7/2}$ binding energy of 86.3−87.7 eV.[41] The Au^{3+} state may possibly correspond with $Au(OH)_3$.[41] In a study of thermal catalytic DPM oxidation on Au-impregnated ZnO catalysts, Corro et al. suggested that Au^0 and Au^{3+} surface sites have two enhancement effects on DPM oxidation, where Au^{3+} moieties enhance the contact efficiency of DPM on Au^{3+} sites, and Au^0 sites enhance the generation of superoxide species at the Au and Zn interface.[42]

The atomic ratios of $Au^{3+}/(Au^{3+} + Au^0)$ calculated from the areas under the deconvolved XPS Au $4f_{7/2}$ spectra corresponding to the Au^0 and Au^{3+} states of the $Au/CaSO_4/\gamma\text{-}Al_2O_3$ and $Au/\gamma\text{-}Al_2O_3$ catalysts (Table S1) demonstrate that the ratio obtained for the $Au/CaSO_4/\gamma\text{-}Al_2O_3$ catalyst (13.6%) was substantially higher than that obtained for the $Au/\gamma\text{-}Al_2O_3$ catalyst (1.15%). This implies that $CaSO_4$ enhances the formation of Au^{3+} sites, which may enhance the contact efficiency of DPM on the $Au/CaSO_4/\gamma\text{-}Al_2O_3$ catalyst surface.

The XPS O 1s spectra obtained for $\gamma\text{-}Al_2O_3$, $Au/\gamma\text{-}Al_2O_3$, $CaSO_4/\gamma\text{-}Al_2O_3$, and $Au/CaSO_4/\gamma\text{-}Al_2O_3$ catalysts (Figure S7b and Table S2) exhibit a number of oxygen valence states. The high-intensity peak in the range of 530.6−530.7 eV can be associated with lattice oxygen (O_{latt}) on $\gamma\text{-}Al_2O_3$ catalyst surfaces,[43] while the peak in the range of 531.5−531.6 eV can be associated with the O atoms in hydroxyl groups (O_{OH}) bonding with Al atoms.[44] According to the literature,[45] the impregnation of $CaSO_4$ in $\gamma\text{-}Al_2O_3$ generated a new peak at 532.0 eV, which was assigned to sulfur-containing functional groups in $CaSO_4$. It was also found that the impregnation of Au alone in $\gamma\text{-}Al_2O_3$ could promote the transformation of O_{latt} to surface O_{OH}, from 54% ($\gamma\text{-}Al_2O_3$) to 60% ($Au/\gamma\text{-}Al_2O_3$). When $CaSO_4$ is present, O_S was found, which has almost the same ratio as O_{OH}. Generally, the total ratios of (O_{OH} and O_S) on $CaSO_4/\gamma\text{-}Al_2O_3$ and $Au/CaSO_4/\gamma\text{-}Al_2O_3$ catalysts are around 60%, which are also higher than that on $\gamma\text{-}Al_2O_3$. This indicated that the surface oxidation capacity of $\gamma\text{-}Al_2O_3$ with Au and $CaSO_4$ is higher than that of pure $\gamma\text{-}Al_2O_3$. The XPS S 2p spectra obtained for the $CaSO_4/\gamma\text{-}Al_2O_3$ and $Au/CaSO_4/\gamma\text{-}Al_2O_3$ catalysts (Figure S7c) indicate that the S $2p_{3/2}$ and S $2p_{1/2}$ binding energies of both catalysts were observed at 169.8 and 169.9 eV, respectively.[46]

The results presented thus far indicate that both Au and $CaSO_4$ can enhance the adsorption of oxygen species on the catalyst surface at temperatures lower than 300 °C and increase the acidity of active catalyst sites. Moreover, the coexistence of Au and $CaSO_4$ produces the best effect, with $Au/CaSO_4/\gamma\text{-}Al_2O_3$ having the highest surface oxidation capacity.

2.2. Plasma-Assisted Catalytic Oxidation of Graphite.

In order to study the feasibility of graphite in this study, the Raman spectrum of graphite carbon powder was collected with a 633 nm laser; the results are shown in Figure S8. Two Raman peaks located at 1578 and 1328 cm^{-1} are designated as G and D bands, respectively. The highest peak at 1578 cm^{-1} can be ascribed to the stretching mode of E_{2g} symmetry. The peak at 1328 cm^{-1} can be considered to be the A_{1g} symmetry stretching, which is ascribed to the disordered carbon structure, indicating that there is a disordered or defective carbon structure in the graphite sample.[47] At the same time, the intensity ratio (I_D/I_G) of D and G peaks of graphite was about 0.3 in this study, which was evidence of the presence of disordered carbon in graphite, those that also exist in DPM.[48,49] Together with the fact that the specific surface area of graphite is close to that of DPM,[50] graphite is used as a simulated DPM to show the oxidation mechanism of carbon.

In order to understand the key role of plasma in graphite oxidation, the control experiments of graphite oxidation without plasma were carried out by the in situ DRIFTS technique (Figure S9). Results suggested that as the reaction time passed, no relevant peak changes were found. This means that even at a high temperature of 200 °C, graphite is difficult to be oxidized in the presence of one catalyst. Then, plasma was introduced into the reaction system and combined with γ-

https://doi.org/10.1021/acsomega.1c06659
ACS Omega 2022, 7, 8640−8650

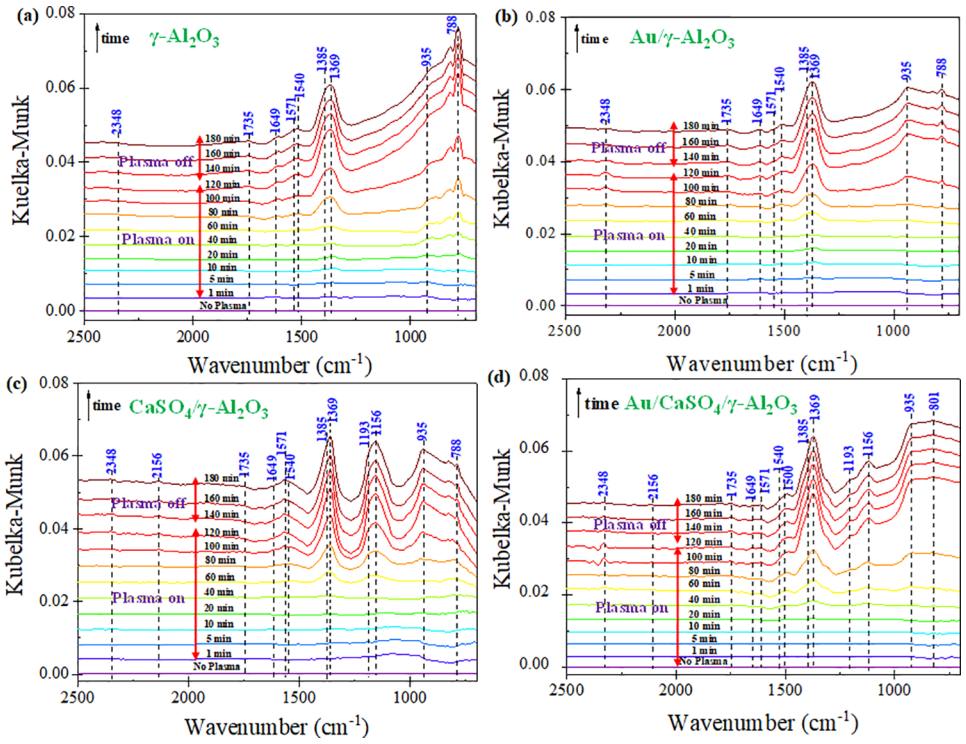

Figure 2. Kubelka–Munk absorption spectra derived from the DRIFTS results obtained at different reaction times during the plasma-assisted catalytic oxidation of graphite with different catalysts (a) γ-Al_2O_3, (b) Au/γ-Al_2O_3, (c) $CaSO_4$/γ-Al_2O_3, and (d) Au/$CaSO_4$/γ-Al_2O_3. Experimental conditions: KBr/catalyst/graphite ratio of 100:10:1 by mass, temperature: 200 °C, inlet gas composition: 10% O_2 (He balance), discharge power: 0.1 W (plasma on).

Al_2O_3, Au/γ-Al_2O_3 $CaSO_4$/γ-Al_2O_3, and Au/$CaSO_4$/γ-Al_2O_3, respectively. The in situ DRIFTS spectra of the graphite sample as a function of discharge time at 200 °C are shown in Figure 2a–d. After discharge, the peaks at 788, 935, 1156, 1193, 1369, 1385, 1540, 1571, 1649, 1735, 2156, and 2348 cm^{-1} were found, indicating that it was easy to form various key intermediates on the surface of the catalyst to promote graphite oxidation under plasma conditions. Detailed information regarding the various related functional groups has been summarized in Table S3.

Of particular importance for the analysis of catalytic graphite oxidation are the three types of SOCs associated with absorption peaks at 935, 1571, and 1735 cm^{-1}, which respectively correspond to the ether −COC− group in epoxy,[51] the −C═O− group in quinone,[52,53] and the carboxylate carbonate −COO− group in lactone[51] that forms during the oxidation of graphite. The heights of these peaks are respectively plotted in Figure 3a–c as a function of reaction time. The peak heights of all three SOCs corresponding to the four catalysts gradually increase with discharge time in the order of Au/$CaSO_4$/γ-Al_2O_3 > $CaSO_4$/γ-Al_2O_3 > Au/γ-Al_2O_3 > γ-Al_2O_3. The observed order is consistent with the orders observed with respect to active site acidity (Figure S5) and surface oxygen adsorption (Figure S6), which verifies that Au/$CaSO_4$, $CaSO_4$, and Au indeed exert catalytic effects with respect to graphite oxidation. However, the absorption peak heights of all SOCs remained constant when plasma discharge was discontinued. Accordingly, the oxidation of graphite also ceased at the termination of plasma discharge, which illustrates the essential role played by plasma discharge in the catalytic oxidation process.

An analysis of the functional groups on the catalyst surfaces is more complicated than for the SOCs associated with graphite oxidation. The heights of the absorption peaks associated with the functional groups on the catalyst surfaces are plotted in Figure 4a–h as a function of reaction time. In general, the peak heights associated with these functional groups typically increase throughout the 120 min period of plasma discharge but then decrease after the termination of plasma discharge. The observed decrease in peak heights after the termination of plasma discharge indicates that these functional groups were unstable. These functional groups are considered individually below.

The characteristic peak at 788 cm^{-1} (Figure 4a) corresponds to the basic oxygen ion (M^+−O−3) at weak Lewis acid sites on the catalyst surfaces.[54−57] The peak height of M^+−O−3 on γ-Al_2O_3 is obviously higher than that of these functional groups on the Au/γ-Al_2O_3, $CaSO_4$/γ-Al_2O_3, and Au/$CaSO_4$/γ-Al_2O_3 catalysts. This indicates that the O_3 groups on the γ-Al_2O_3 surfaces were less reactive than those on the Au/γ-Al_2O_3, $CaSO_4$/γ-Al_2O_3, and Au/$CaSO_4$/γ-Al_2O_3 surfaces. The characteristic peak at 1369 cm^{-1} (Figure 4b) corresponds to O atoms bonded to active Lewis acid sites on the catalyst surfaces, resulting in the formation of M−O.[55,57,58] These O atoms can be expected to have derived from O_3 decomposition during the period of plasma discharge. The peak heights associated with the M−O groups also uniformly decrease with the different catalysts in the order of Au/$CaSO_4$/γ-Al_2O_3 > $CaSO_4$/γ-Al_2O_3 > Au/γ-Al_2O_3 > γ-Al_2O_3, which implies that Au/$CaSO_4$, $CaSO_4$, and Au promote O_3 decomposition (as M^+−O−3) to form M−O groups. The characteristic peak at 1385 cm^{-1} (Figure 4c) is attributed to the asymmetric stretching mode of carboxyl carbonate (M−C(═O)O−).[57]

https://doi.org/10.1021/acsomega.1c06659
ACS Omega 2022, 7, 8640−8650

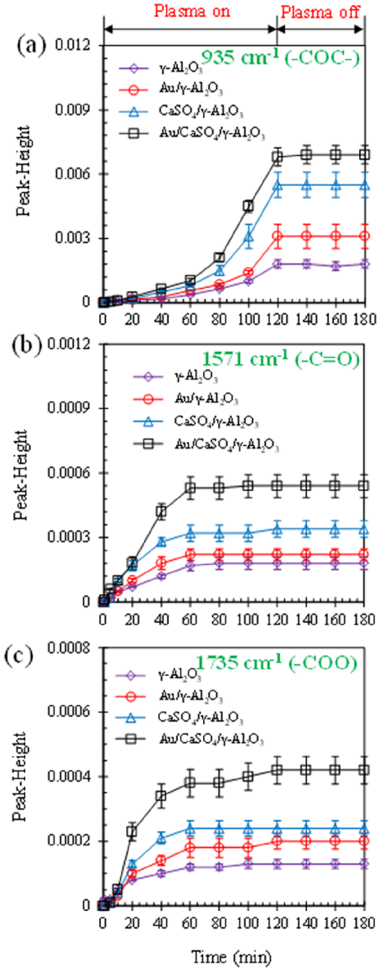

Figure 3. Peak heights of absorption spectra associated with SOC groups (a) −COC−, (b) −C═O, and (c) −COO− arising from graphite oxidation as a function of reaction time. Data are presented as mean ± standard error of the mean (SEM).

The formation of functional groups containing carbon obviously arises due to interactions between the graphite and catalyst surfaces, where oxidized carbon can move from the graphite surface to the catalyst surface. A similar finding has been reported for the catalyzed oxidation of graphite by $CaCO_3$ surfaces.[33] The characteristic peak at 2348 cm^{-1} (Figure 4d) represents gaseous CO_2.[59] Of particular interest here is that the peak heights decreased rapidly to zero when plasma discharge was terminated. While gaseous CO_2 diffusing into the infrared radiation (IR) beam path can yield an instrument response, this is mitigated by the gas flow passing the catalyst sample through the narrow discharge gap. The absorption peak heights associated with gaseous CO_2 during the plasma discharge period decrease with the different catalysts in the order of $Au/CaSO_4/\gamma\text{-}Al_2O_3$ > $CaSO_4/\gamma\text{-}Al_2O_3$ > $Au/\gamma\text{-}Al_2O_3$ > $\gamma\text{-}Al_2O_3$. Accordingly, the CO_2 concentrations produced from these catalysts decrease in the same order because the peak height is proportional to the CO_2 concentration. This finding also demonstrates that the formation of M−O and M−COO− is favorable for oxidizing graphite to gaseous CO_2.

The characteristic peaks at 1540 and 1649 cm^{-1} (Figure 4e,f, respectively) are associated with a monodentate carbonate M−O−(CO_2) group[60] and a bicarbonate M−OH(CO_2) group,[61] respectively. Here, the M−O−(CO_2) groups were formed from the gaseous CO_2 derived from graphite oxidation and the M−O sites on the alumina surface.[62] The bicarbonate M−OH(CO_2) was formed from the gaseous CO_2 and M−OH sites on the alumina surface.[57] Here, the M−OH sites were produced via the following previously proposed reaction.[63]

$$M\text{−}OH_2 + O \rightarrow M\text{−}OH \quad (1)$$

Both peak heights associated with the M−O−(CO_2) and M−OH(CO_2) groups uniformly increase with the different catalysts in the order of $Au/CaSO_4/\gamma\text{-}Al_2O_3$ < $CaSO_4/\gamma\text{-}Al_2O_3$ < $Au/\gamma\text{-}Al_2O_3$ < $\gamma\text{-}Al_2O_3$, which is diametrically opposite to that observed for the formation of gaseous CO_2 (i.e., $Au/CaSO_4/\gamma\text{-}Al_2O_3$ > $CaSO_4/\gamma\text{-}Al_2O_3$ > $Au/\gamma\text{-}Al_2O_3$ > $\gamma\text{-}Al_2O_3$). This suggests that the M−O−(CO_2) and M−OH(CO_2) groups are the intermediates of gaseous CO_2 formation, where the lowest concentrations of M−O−(CO_2) and M−OH(CO_2) on $Au/CaSO_4/\gamma\text{-}Al_2O_3$ correspond to the highest activity of $Au/CaSO_4/\gamma\text{-}Al_2O_3$ for enhancing the gasification of M−O−(CO_2) and M−OH(CO_2) to form gaseous CO_2.

The characteristic peaks at 1156 and 1193 cm^{-1} (Figure 4g,h, respectively) are associated with $CaSO_4$ species[64−66] and the asymmetric stretching vibrations of S═O,[67,68] respectively. All peak heights increased with increasing reaction time during plasma discharge and became constant after the termination of plasma discharge. The increase in peak heights is obviously due to the oxidative removal of graphite from the surfaces of $CaSO_4$ molecules, resulting in an increased proportion of $CaSO_4$ reflecting IR light. Moreover, the peak heights associated with S═O stretching vibrations remained constant after the termination of plasma discharge because no graphite oxidation occurred during this period, as demonstrated by the results in Figure 3.

The MS signals associated with CO_2 content in the outlet gas of the in situ cell are plotted in Figure 5 as a function of reaction time. The MS signal of CO_2 obtained in conjunction with the $\gamma\text{-}Al_2O_3$ catalyst increased rapidly at the initiation of plasma discharge and obtained the highest CO_2 signal over the first 20 min of plasma discharge. However, the CO_2 signal decreased on average thereafter. While similar CO_2 MS signal behaviors were observed in conjunction with the $Au/\gamma\text{-}Al_2O_3$, $CaSO_4/\gamma\text{-}Al_2O_3$, and $Au/CaSO_4/\gamma\text{-}Al_2O_3$ catalysts, all three CO_2 signals began uniformly increasing on average after 20−40 min of plasma discharge. The general magnitudes of the CO_2 MS signals observed for all four catalysts after about 40 min of plasma discharge decreased in the order of $Au/CaSO_4/\gamma\text{-}Al_2O_3$ > $CaSO_4/\gamma\text{-}Al_2O_3$ > $Au/\gamma\text{-}Al_2O_3$ > $\gamma\text{-}Al_2O_3$, which is the same order as that of the concentration of gaseous CO_2 obtained in the in situ cell by DRIFTS (Figure 4d).

The very different trends observed for the MS signals of CO_2 obtained over time for the catalysts with and without Au or $CaSO_4$ are interesting. In this regard, two main oxidation processes have been observed during graphite oxidation, including the oxidation of surface carbon atoms and intercalated carbon atoms.[69] Accordingly, the different trends observed in Figure 5 are possibly due to the fact that surface carbon atoms have been shown to be easily oxidized, while the oxidation of intercalated carbons to CO_2 is difficult[70] because the carbon incorporated with oxygen is more readily oxidized.[53,71] In addition, the formation of M−COO− groups may play an important role for graphite oxidation because the absorption peak heights associated with these groups were observed to increase dramatically after 20 min of plasma

https://doi.org/10.1021/acsomega.1c06659
ACS Omega 2022, 7, 8640−8650

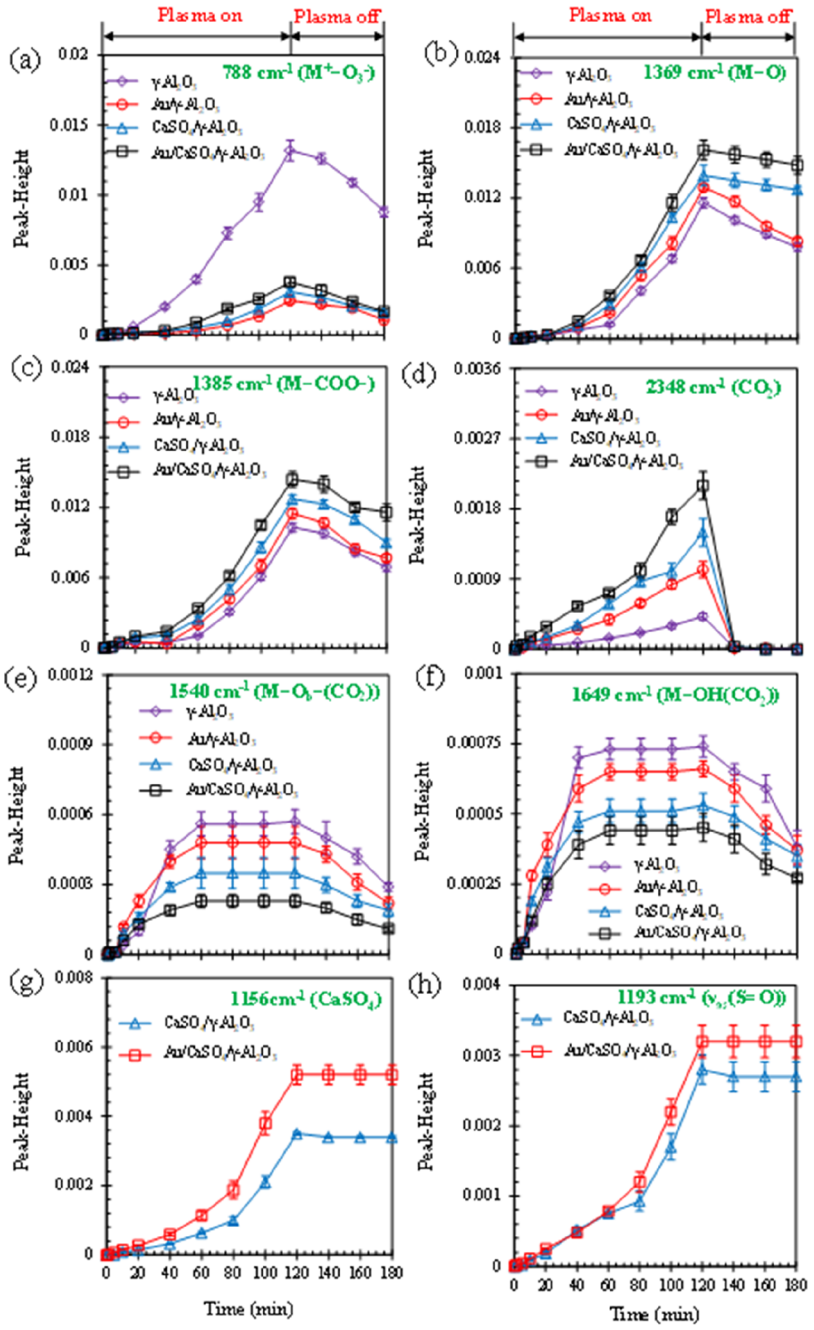

Figure 4. Peak heights of absorption spectra associated with the different surface functional groups (a) M^+-O-3, (b) M−O, (c) M−COO−, (d) CO_2, (e) $M-O_b-(CO_2)$, (f) $M-OH(CO_2)$, (g) $CaSO_4$, and (h) $\nu_{as}(S{=}O)$ of γ-Al_2O_3, Au/γ-Al_2O_3, $CaSO_4$/γ-Al_2O_3, and Au/$CaSO_4$/γ-Al_2O_3 catalysts as a function of reaction time. Data are presented as mean ± SEM.

discharge (Figure 4c), which is similar to the trends observed for the MS signals of CO_2 (Figure 5). Finally, as shown in Figure 4e,f, the peak heights associated with the $M-O-(CO_2)$ and $M-OH(CO_2)$ groups are lowest for the γ-Al_2O_3 catalyst in the first 20 min and then greatest for the γ-Al_2O_3 catalyst thereafter. Accordingly, it can be speculated that CO_2 was the least sequestered at these sites on the surface of the γ-Al_2O_3 catalyst in the first 20 min and the most sequestered at these sites thereafter.

2.3. Effects of $CaSO_4$ and Au. The mechanisms by which Au and $CaSO_4$ promote the catalytic oxidation of graphite can be more fully analyzed from the Kubelka−Munk absorption spectra derived from the DRIFTS results obtained at different reaction times with Au/γ-Al_2O_3, $CaSO_4$/γ-Al_2O_3, Au/$CaSO_4$/γ-Al_2O_3, and pure $CaSO_4$ catalysts at 200 °C, which are presented in Figure S10 in the wavenumber range of 725 to 1500 cm^{-1}. The absorption peaks observed at 788, 844, 1034, 1124, and 1369 cm^{-1} correspond to M^+-O-3, S−O,[72,73] S═O, M^+-O-2, and M−O groups, respectively (Table S3).

The peak heights of the absorption spectra associated with the S−O, S═O, M^+-O-2, and M−O functional groups of the four catalysts considered are presented as a function of reaction time in Figure 6a−d, respectively. Except for the peaks associated with the S═O group (Figure 6b), the peak heights invariably increased with increasing plasma discharge time but decreased after the termination of plasma discharge. Again, the

https://doi.org/10.1021/acsomega.1c06659
ACS Omega 2022, 7, 8640−8650

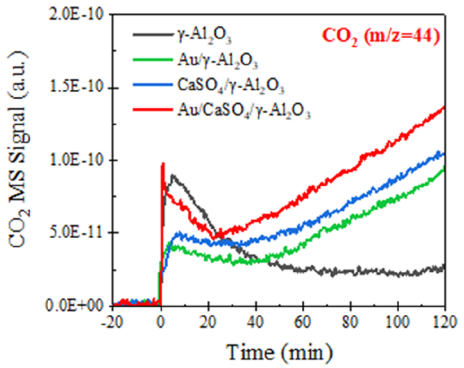

Figure 5. MS signals of CO_2 in the outlet gas obtained with different catalysts plotted with respect to reaction time before and during the period of plasma discharge. Experimental condition: catalyst/graphite ratio of 20:1 by mass.

observed decrease in peak heights after the termination of plasma discharge indicates that these functional groups were unstable. This is particularly the case for the peak heights associated with the M^+-O-2 groups,[74] which decrease to nearly zero within the 60 min period after the termination of plasma discharge. The presence of Au is observed to promote the formation of S−O, M^+-O- 2, and M−O groups in comparison with the corresponding peak heights obtained by $CaSO_4/\gamma$-Al_2O_3 (Figure 6a,c,d). The contrary behavior of the peak heights associated with the S═O groups observed with respect to reaction time (Figure 6b) can be explained by noting that the S−O groups were generated from the S═O groups,[68] which may possibly conform to the following reaction, where the S atoms in the $CaSO_4$ components were strictly present in only the S^{6+} state.[75]

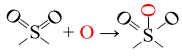

(2)

Accordingly, the observed increase in the peak heights associated with S═O after the termination of plasma discharge mirrors the observed decrease in the peak heights associated with S−O, where the reverse reaction would form S═O from the S−O groups. In addition, Au can decompose O_3 to O via the following reaction.

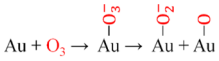

(3)

2.4. Mechanism of Graphite Oxidation Catalyzed by $CaSO_4$ and Au. The mechanism associated with the plasma-assisted catalytic oxidation of graphitic carbon with Au/$CaSO_4/\gamma$-Al_2O_3 catalysts based on the above experimental results is illustrated in Figure 7. Impacts between O_2 molecules in the discharge space with the energetic electrons and ions induced by plasma discharge decompose the O_2 molecules to form O atoms and O_3 molecules, which can be adsorbed on the Lewis acid (or base) sites on the surface of γ-Al_2O_3 to form M−O and M^+-O- 3 functional groups, respectively. In addition, the three types of SOCs (i.e., −COC−, −C═O−, and −COO−) are generated on the graphite surface. Here, the terminal carbon atoms on the graphite surface are first oxidized to −COO− and −C═O. The interactions of O atoms with carbon atoms in the graphite rings result in the formation of −COC− by destroying the C═C groups. This open-ring reaction is promoted by M−O groups on the catalyst surface, where the formation of these groups is enhanced by the presence of Au or $CaSO_4$. Here, Au can decompose O_3 to O, whereas $CaSO_4$ can save and release O atoms. The oxidation of opened ring carbons to CO_2 continues via the formation of

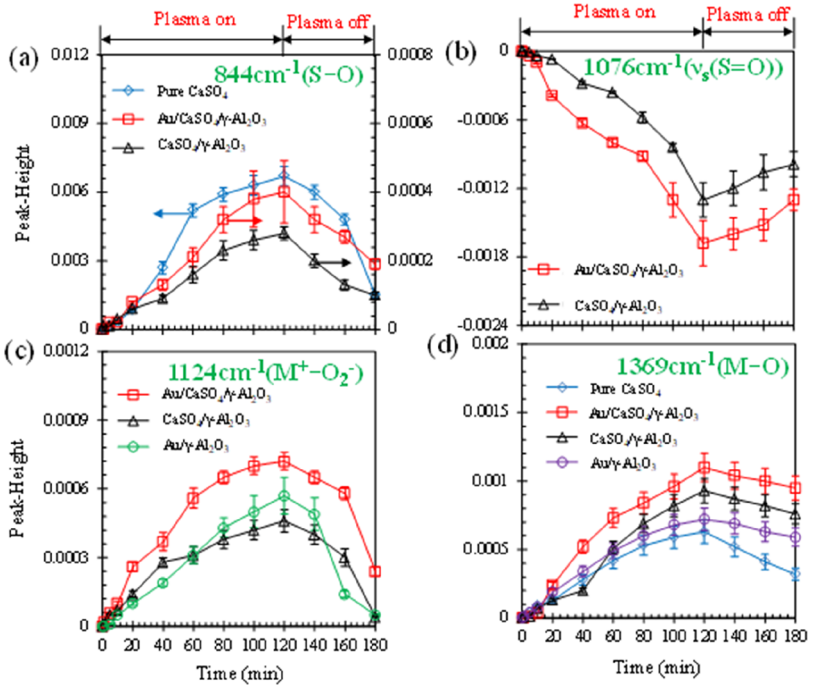

Figure 6. Peak heights of absorption spectra associated with the different surface functional groups (a) S−O, (b) ν_s(S=O), (c) M^+-O-2, and (d) M−O of Au/γ-Al_2O_3, $CaSO_4/\gamma$-Al_2O_3, Au/$CaSO_4/\gamma$-Al_2O_3, and pure $CaSO_4$ catalysts as a function of reaction time. Data are presented as mean ± SEM.

https://doi.org/10.1021/acsomega.1c06659
ACS Omega 2022, 7, 8640−8650

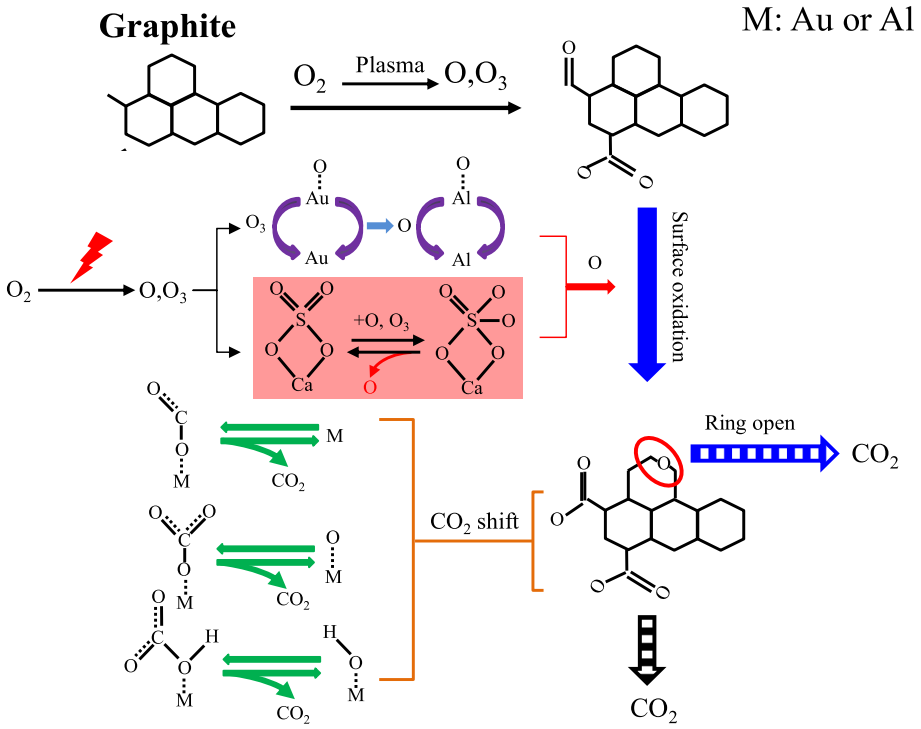

Figure 7. Proposed mechanism of plasma-assisted graphite oxidation catalyzed by $CaSO_4$ and Au.

−COO− and −C═O. Finally, the M−O and M−OH groups also facilitate graphite oxidation to CO_2 by catalyzing the SOCs moving from the graphite surface to the catalyst surface to form M−O−(CO_2) and M−OH(CO_2) groups, respectively.

3. CONCLUSIONS

The present study addressed the poorly understood role sulfates play in the promotion of DPM oxidation in a plasma-assisted context by investigating the underlying mechanisms of DPM oxidation during plasma-assisted catalytic processes using graphitic carbon in conjunction with γ-Al_2O_3, $CaSO_4$/γ-Al_2O_3, Au/γ-Al_2O_3, and Au/$CaSO_4$/γ-Al_2O_3 catalysts. Considerable detail was obtained during in situ analyses of the plasma-assisted catalytic oxidation process of graphite based on DRIFTS and MS data collected before, during, and after the application of 120 min of continuous plasma discharge. The main results are summarized as follows: (1) Au and $CaSO_4$ can enhance graphite oxidation; (2) Au was found to promote the decomposition of O_3 to O to form M−O groups on the catalyst surface; (3) $CaSO_4$ was found to promote graphite oxidation by reversibly saving and releasing O atoms via its −S═O units; (4) in the proposed mechanism, graphite is firstly oxidized to −COO− and −C═O; (5) the O atoms react with carbon atoms in the graphite rings, resulting in the formation of −COC−; (6) the Au or $CaSO_4$ impregnated catalysts also promote the movement of carbonates from the graphite surfaces to the catalyst surfaces, followed by the formation of CO_2 from the gasification of surface carbonates. These findings clearly improve the understanding of the plasma-assisted catalytic oxidation mechanisms of DPM and further support the development of efficient plasma-assisted catalysts.

4. EXPERIMENTAL SECTION

4.1. Catalyst Preparation and Characterization. Four types of catalysts (Au/$CaSO_4$/γ-Al_2O_3, $CaSO_4$/γ-Al_2O_3, Au/γ-Al_2O_3, and γ-Al_2O_3) were prepared using methods described in the Supporting Information. These obtained catalysts were characterized using transmission electron microscopy (TEM; FEI Talos F200s, ThermoFisher), NH_3-TPD (BelCata II, MicrotracBEL), and O_2-TPD. The distributions of major elements were determined using EDS. XPS (Nexsa, ThermoFisher) was employed to investigate the chemical properties of the catalyst surfaces. In addition, the Raman spectrum (Raman, LabRAM HR800, Horiba Jobin Yvon) was used to analyze the state and properties of the graphite microstructure surface. The obtained characterization results are presented in the Supporting Information.

4.2. In Situ DRIFTS Coupled with DBD and MS Characterization. The in situ DRIFTS−MS system with the fluidized bed reactor and DBD plasma cell are illustrated in Figure 1. The system consists of gas cylinders, mass flow meters (MFCs; Sevenstars), a DRIFTS instrument (Nicolet is50, Thermo Scientific), a mass spectrometer (LC-D200, TILON), and a pulse power supply (M10K-08, Suzhou Allftek). The DRIFTS instrument was equipped with an in situ cell (HVC-DRP-5, Harrick) and a narrow-band mercury cadmium telluride (MCT-A) detector with liquid nitrogen cooling for high sensitivity (0.09 cm^{-1}) when collecting DRIFTS spectra between 4000 and 650 cm^{-1}. The in situ cell was installed with a DBD unit over the catalyst sample. The DBD unit was mainly composed of a quartz tube [2 mm (o.d.) × 1 mm (i.d.) × 15 mm (length)] and a stainless steel rod [1 mm (o.d.) × 20 mm (length)]. The stainless steel rod was connected to the high voltage terminal of the pulse power supply, while the body of the in situ cell was connected to the ground terminal of the pulse power supply. The gap distance between the front of the sealed quartz tube and the catalyst

https://doi.org/10.1021/acsomega.1c06659
ACS Omega 2022, 7, 8640−8650

surface was 0.5 mm, and pulsed corona discharges occurred within the gap space during the application of voltage pulses between the stainless steel rod and the body of the in situ cell. The waveforms of the applied voltage and current were measured using a voltage probe (P6015A, Tektronix), current probe (CP8030H, Cybertek), and digital fluorescent oscilloscope (DPO 3034, Tektronix). The typical applied voltage and current waveforms are presented in Figure S1.

The particle size of the graphite carbon powder used in the experiment is within the range of normal diesel engine soot particles (10 nm to 1 μm).[2] TEM images of the graphitic carbon are presented in Figure S2. The graphite powder samples were mixed with KBr (spectral grade, >99.5% purity, Shanghai Gexiang, China) and the catalyst powder in a KBr/catalyst/graphite ratio of 100:10:1 by weight. About 30 mg of the mixed powder sample was loaded into the in situ cell.

Prior to collecting DRIFTS spectra, all powder samples in the in situ cell were pretreated at 500 °C in helium (He, 20 mL/min, purity 99.999%, Huayang, Changzhou, China) for 1 h, cooled to 200 °C, and held stable at that temperature for 20 min. A temperature of 200 °C was uniformly applied during all subsequent reaction processes. This temperature was adopted as it was a typical temperature of the exhaust gas from a diesel engine.[76] Finally, the background spectra were collected. Then, the in situ cell was fed with a mixture of 10 vol % O_2 (2 mL/min, purity 99.999%, Huayang, Changzhou, China) with a remainder of He (18 mL/min) for about 10 min. Finally, DRIFTS spectra were collected at 0 min (i.e., without plasma discharge) and at regular intervals of time after the commencement of plasma discharge. Plasma discharge was applied for 120 min and then discontinued while DRIFTS spectra were collected over an additional period of 60 min. This resulted in the collection of a total of 32 scans for each DRIFTS spectrum at a resolution of 4 cm^{-1}, and the DRIFTS spectra were subsequently analyzed using OMNIC software. All DRIFTS spectra obtained were transformed into absorption spectra by the use of the Kubelka−Munk function, which is linearly related to the absorbent concentration in a DRIFTS spectrum.[77] Meanwhile, MS analysis was conducted simultaneously and continuously with the collection of DRIFTS spectra to determine the concentration of CO_2 in the gas outflowing from the in situ cell. The DRIFTS spectrum of each catalyst under each experimental condition was determined at least in triplicate.

■ ASSOCIATED CONTENT

Supporting Information

The Supporting Information is available free of charge at https://pubs.acs.org/doi/10.1021/acsomega.1c06659.

Plasma discharge voltage and current waveforms employed, characterizations of catalysts and graphitic carbon powders, and summaries of the characteristic peaks and functional groups observed in DRIFTS spectra (PDF)

■ AUTHOR INFORMATION

Corresponding Authors

Shuiliang Yao − *School of Environmental and Safety Engineering, Advanced Plasma Catalysis Engineering Laboratory for China Petrochemical Industry, Changzhou University, Changzhou, Jiangsu 213164, China;* orcid.org/0000-0001-5142-1735; Email: yaos@cczu.edu.cn

Jiali Zhu − *School of Environmental and Safety Engineering, Advanced Plasma Catalysis Engineering Laboratory for China Petrochemical Industry, Changzhou University, Changzhou, Jiangsu 213164, China*; Email: zhujl@cczu.edu.cn

Authors

Chengrong Kong − *School of Environmental and Safety Engineering, Advanced Plasma Catalysis Engineering Laboratory for China Petrochemical Industry, Changzhou University, Changzhou, Jiangsu 213164, China*

Zuliang Wu − *School of Environmental and Safety Engineering, Advanced Plasma Catalysis Engineering Laboratory for China Petrochemical Industry, Changzhou University, Changzhou, Jiangsu 213164, China*

Jing Li − *School of Environmental and Safety Engineering, Advanced Plasma Catalysis Engineering Laboratory for China Petrochemical Industry, Changzhou University, Changzhou, Jiangsu 213164, China; Engineering Research Center of Construction Technology of Precast Concrete of Zhejiang Province, Hangzhou 310018, China*

Guojian Li − *School of Environmental and Safety Engineering, Advanced Plasma Catalysis Engineering Laboratory for China Petrochemical Industry, Changzhou University, Changzhou, Jiangsu 213164, China; Engineering Research Center of Construction Technology of Precast Concrete of Zhejiang Province, Hangzhou 310018, China*

Complete contact information is available at: https://pubs.acs.org/10.1021/acsomega.1c06659

Notes

The authors declare no competing financial interest.

Data availability: The experimental data are available upon request to the corresponding authors.

■ ACKNOWLEDGMENTS

This research was supported by the National Natural Science Foundation of China (grant no. 12075037), the Open Foundation of Engineering Research Center of Construction Technology of Precast Concrete of Zhejiang Province (grant no. ZZP1902), and the Postgraduate Research & Practice Innovation Program of Jiangsu Province (grant no. SJCX20_0934).

■ REFERENCES

(1) Beniya, A.; Higashi, S. Towards dense single-atom catalysts for future automotive applications. *Nat. Catal.* **2019**, *2*, 590−602.

(2) Neha; Prasad, R.; Singh, S. V. A review on catalytic oxidation of soot emitted from diesel fuelled engines. *J. Environ. Chem. Eng.* **2020**, *8*, 103945.

(3) Bengalli, R.; et al. In vitro pulmonary and vascular effects induced by different diesel exhaust particles. *Toxicol. Lett.* **2019**, *306*, 13−24.

(4) Luján, J. M.; Bermúdez, V.; Dolz, V.; Monsalve-Serrano, J. An assessment of the real-world driving gaseous emissions from a Euro 6 light-duty diesel vehicle using a portable emissions measurement system (PEMS). *Atmos. Environ.* **2017**, *174*, 112−121.

(5) Vijayaraghavan, K.; Lindhjem, C.; Koo, B.; Denbleyker, A.; Tai, E.; Shah, T.; Alvarez, Y.; Yarwood, G. Source apportionment of emissions from light-duty gasoline vehicles and other sources in the United States for ozone and particulate matter. *J. Air Waste Manage.* **2016**, *66*, 98−119.

(6) Jang, J.; Lee, Y.; Kwon, O. Comparison of fuel efficiency and exhaust emissions between the aged and new DPF systems of Euro 5 diesel passenger car. *Int. J. Automot. Technol.* **2017**, *18*, 751−758.
(7) Mokhri, M. A.; Abdullah, N. R.; Abdullah, S. A.; Kasalong, S.; Mamat, R. Soot filtration recent simulation analysis in diesel particulate filter (DPF). *Procedia Eng.* **2012**, *41*, 1750−1755.
(8) Pu, X.; Cai, Y.; Shi, Y.; Wang, J.; Gu, L.; Tian, J.; Cui, Y. Test on diesel particulate filter regeneration using non-thermal plasma technology aided by exhaust waste heat. *Trans. Chin. Soc. Agric. Eng.* **2017**, *33*, 70−77.
(9) Wagloehner, S.; Nitzer-Noski, M.; Kureti, S. Oxidation of soot on manganese oxide catalysts. *Chem. Eng. J.* **2015**, *259*, 492−504.
(10) Nossova, L.; Caravaggio, G.; Couillard, M.; Ntais, S. Effect of preparation method on the performance of silver-zirconia catalysts for soot oxidation in diesel engine exhaust. *Appl. Catal., B* **2018**, *225*, 538−549.
(11) Preble, C. V.; Dallmann, T. R.; Kreisberg, N. M.; Hering, S. V.; Harley, R. A.; Kirchstetter, T. W. Effects of particle filters and selective catalytic reduction on heavy-duty diesel drayage truck emissions at the port of Oakland. *Environ. Sci. Technol.* **2015**, *49*, 8864−8871.
(12) Chong, H. S.; Aggarwal, S. K.; Lee, K. O.; Yang, S. Y. Measurements of heat release of diesel PM for advanced thermal management strategies for DPF regeneration. *Combust. Sci. Technol.* **2011**, *183*, 1328−1341.
(13) Fino, D.; Bensaid, S.; Piumetti, M.; Russo, N. A review on the catalytic combustion of soot in Diesel particulate filters for automotive applications: From powder catalysts to structured reactors. *Appl. Catal., A* **2016**, *509*, 75−96.
(14) Yao, S.; Shen, X.; Zhang, X.; Han, J.; Wu, Z.; Tang, X.; Lu, H.; Jiang, B. Sustainable removal of particulate matter from diesel engine exhaust at low temperature using a plasma-catalytic method. *Chem. Eng. J.* **2017**, *327*, 343−350.
(15) Yao, S. Plasma reactors for diesel particulate matter removal. *Recent Pat. Chem. Eng.* **2009**, *2*, 67−75.
(16) Gao, J.; Ma, C.; Xing, S.; Sun, L.; Huang, L. Nanostructure analysis of particulate matter emitted from a diesel engine equipped with a NTP reactor. *Fuel* **2017**, *192*, 35−44.
(17) Shi, Y.; Cai, Y.; Li, X.; Xu, H.; Li, W.; Pu, X. Low temperature diesel particulate filter regeneration by atmospheric air non-thermal plasma injection system. *Plasma Chem. Plasma Process.* **2016**, *36*, 783−797.
(18) Tang, T.; Zhang, J.; Cao, D.; Shuai, S.; Zhao, Y. Experimental study on filtration and continuous regeneration of a particulate filter system for heavy-duty diesel engines. *J. Environ. Sci.* **2014**, *26*, 2434−2439.
(19) Yamamoto, S.; Yao, S.; Kodama, S.; Mine, C.; Fujioka, Y. Investigation of transition metal oxide catalysts for diesel PM removal under plasma discharge conditions. *Open Catal. J.* **2008**, *1*, 11−16.
(20) Sekine, Y.; Koyama, H.; Matsukata, M.; Kikuchi, E. Plasma-assisted oxidation of carbon particle by lattice oxygen on/in oxide catalyst. *Fuel* **2013**, *103*, 2−6.
(21) Ranji-Burachaloo, H.; Masoomi-Godarzi, S.; Khodadadi, A. A.; Mortazavi, Y. Synergetic effects of plasma and metal oxide catalysts on diesel soot oxidation. *Appl. Catal., B* **2016**, *182*, 74−84.
(22) Yao, S.; Suzuki, E.; Nakayama, A. Oxidation of activated carbon and methane using a high-frequency pulsed plasma. *J. Hazard. Mater.* **2001**, *83*, 237−242.
(23) Corro, G.; Fierro, J. L. G.; Odilon, V. C. An XPS evidence of Pt^{4+} present on sulfated Pt/Al_2O_3 and its effect on propane combustion. *Catal. Commun.* **2003**, *4*, 371−376.
(24) De Rivas, B.; Sampedro, C.; García-Real, M.; López-Fonseca, R.; Gutiérrez-Ortiz, J. I. Promoted activity of sulphated Ce/Zr mixed oxides for chlorinated VOC oxidative abatement. *Appl. Catal., B* **2013**, *129*, 225−235.
(25) Gu, T.; Liu, Y.; Weng, X.; Wang, H.; Wu, Z. The enhanced performance of ceria with surface sulfation for selective catalytic reduction of NO by NH_3. *Catal. Commun.* **2010**, *12*, 310−313.
(26) Furuta, S.; Matsuhashi, H.; Arata, K. Catalytic action of sulfated tin oxide for etherification and esterification in comparison with sulfated zirconia. *Appl. Catal., A* **2004**, *269*, 187−191.
(27) Yao, S.; Zhang, H.; Shen, X.; Han, J.; Wu, Z.; Tang, X.; Lu, H.; Jiang, B.; Nozaki, T.; Zhang, X. A novel four-way plasma-catalytic approach for the after-treatment of diesel engine exhausts. *Ind. Eng. Chem. Res.* **2018**, *57*, 1159−1168.
(28) Liu, S.; Wu, X.; Weng, D.; Li, M.; Fan, J. Sulfation of Pt/Al_2O_3 catalyst for soot oxidation: High utilization of NO_2 and oxidation of surface oxygenated complexes. *Appl. Catal., B* **2013**, *138*−*139*, 199−211.
(29) Kikugawa, M.; Yamazaki, K.; Kato, A.; Uyama, T.; Takahashi, N.; Shinjoh, H. Silver sulfate catalyst for soot oxidation with high resistance to sulfur poisoning. *Appl. Catal., A* **2019**, *576*, 32−38.
(30) Hao, H.; Jin, B.; Liu, W.; Wu, X.; Yin, F.; Liu, S. Robust Pt@TiO_x/TiO_2 Catalysts for hydrocarbon combustion: Effects of Pt-TiO_x interaction and sulfates. *ACS Catal.* **2020**, *10*, 13543−13548.
(31) Chen, L.; Agrawal, V.; Tait, S. L. Sulfate promotion of selective catalytic reduction of nitric oxide by ammonia on ceria. *Catal. Sci. Technol.* **2019**, *9*, 1802−1815.
(32) Zhang, Z.; Huang, J.; Xia, H.; Dai, Q.; Gu, Y.; Lao, Y.; Wang, X. Chlorinated volatile organic compound oxidation over SO_4^{2-}/Fe_2O_3 catalysts. *J. Catal.* **2018**, *360*, 277−289.
(33) Yao, S.; Zhang, H.; Chen, Z.; Lin, H.; Han, S.; Wu, X.; Dong, R.; Wu, Z.; Nozaki, T. Promotion of graphitic carbon oxidation via stimulating CO_2 desorption by calcium carbonate. *J. Hazard. Mater.* **2019**, *363*, 10−15.
(34) Liu, S.; Wu, X.; Weng, D.; Li, M.; Ran, R. Roles of acid sites on Pt/H-ZSM5 catalyst in catalytic oxidation of diesel soot. *ACS Catal.* **2015**, *5*, 909−919.
(35) Busca, G. Catalytic materials based on silica and alumina: Structural features and generation of surface acidity. *Prog. Mater. Sci.* **2019**, *104*, 215−249.
(36) Varala, R.; Narayana, V.; Kulakarni, S. R.; Khan, M.; Alwarthan, A.; Adil, S. F. Sulfated tin oxide (STO) − Structural properties and application in catalysis: A review. *Arabian J. Chem.* **2016**, *9*, 550−573.
(37) Li, P.; He, C.; Cheng, J.; Ma, C. Y.; Dou, B. J.; Hao, Z. P. Catalytic oxidation of toluene over Pd/Co_3AlO catalysts derived from hydrotalcite-like compounds: Effects of preparation methods. *Appl. Catal., B* **2011**, *101*, 570−579.
(38) Liu, H.; Kozlov, A. I.; Kozlova, A. P.; Shido, T.; Asakura, K.; Iwasawa, Y. Active oxygen species and mechanism for low-temperature CO oxidation reaction on a TiO_2-supported Au catalyst prepared from $Au(PPh_3)(NO_3)$ and As-precipitated titanium hydroxide. *J. Catal.* **1999**, *185*, 252−264.
(39) Mukherjee, D.; Venkataswamy, P.; Devaiah, D.; Rangaswamy, A.; Reddy, B. M. Crucial role of titanium dioxide support in soot oxidation catalysis of manganese doped ceria. *Catal. Sci. Technol.* **2017**, *7*, 3045−3055.
(40) Hao, Z.; Cheng, D.; Guo, Y.; Liang, Y. Supported gold catalysts used for ozone decomposition and simultaneous elimination of ozone and carbon monoxide at ambient temperature. *Appl. Catal., B* **2001**, *33*, 217−222.
(41) Zhao, G.; Gao, E.; Wan, Q.; Liu, Q.; Liang, J.; Qiao, Y.; Zhao, G.; Tian, Y. Structure-activity relationships of Au/Al_2O_3 catalyst for the selective oxidative esterification of 1,3-Propanediol and Methanol. *ChemistrySelect* **2019**, *4*, 12479−12490.
(42) Corro, G.; Cebada, S.; Pal, U.; Fierro, J. L. G. Au^0−Au^{3+} bifunctional site mediated enhanced catalytic activity of Au/ZnO composite in diesel particulate matter oxidation. *J. Catal.* **2017**, *347*, 148−156.
(43) Zhang, Y.; Niu, S.; Han, K.; Li, Y.; Lu, C. Synthesis of the SrO-CaO-Al_2O_3 trimetallic oxide catalyst for transesterification to produce biodiesel. *Renewable Energy* **2021**, *168*, 981−990.
(44) Meza-Arroyo, J.; Chandra Sekhar Reddy, K.; Syamala Rao, M. G.; Garibay-Martínez, F.; de Urquijo-Ventura, M. S.; Ramírez-Bon, R. Solution-based CdS thin film transistors with low temperature-processed Al_2O_3-GPTMS-PMMA as hybrid dielectric gate. *Semicond. Sci. Technol.* **2021**, *36*, 045015.

https://doi.org/10.1021/acsomega.1c06659
ACS Omega 2022, 7, 8640−8650

(45) Christie, A. B.; Sutherland, I.; Walls, J. M. Studies of the composition, ion-induced reduction and preferential sputtering of anodic oxide films on Hg0.8Cd0.2Te by XPS. *Surf. Sci.* **1983**, *135*, 225−242.
(46) Baltrusaitis, J.; Cwiertny, D. M.; Grassian, V. H. Adsorption of sulfur dioxide on hematite and goethite particle surfaces. *Phys. Chem. Chem. Phys.* **2007**, *9*, 5542−5554.
(47) Reich, S.; Thomsen, C. Raman spectroscopy of graphite. *Philos. Trans. R. Soc., A* **2004**, *362*, 2271−2288.
(48) Uy, D.; Ford, M. A.; Jayne, D. T.; ÓNeill, A. E.; Haack, L. P.; Hangas, J.; Jagner, M. J.; Sammut, A.; Gangopadhyay, A. K. Characterization of gasoline soot and comparison to diesel soot: Morphology, chemistry, and wear. *Tribol. Int.* **2014**, *80*, 198−209.
(49) Soewono, A.; Rogak, S. Morphology and Raman spectra of engine-emitted particulates. *Aerosol Sci. Technol.* **2011**, *45*, 1206−1216.
(50) Poster, D. L.; Lopez de Alda, M. J.; Schantz, M. M.; Sander, L. C.; Wise, S. A.; Vangel, M. G. Development and analysis of three diesel particulate-related standard reference materials for the determination of chemical, physical, and biological characteristics. *Polycyclic Aromat. Compd.* **2010**, *23*, 141−191.
(51) Arjunan, V.; Anitha, R.; Devi, L.; Mohan, S.; Yang, H. Comprehensive quantum chemical and spectroscopic (FTIR, FT-Raman, 1H, 13C NMR) investigations of (1,2-epoxyethyl)benzene and (1,2-epoxy-2-phenyl)propane. *Spectrochim. Acta, Part A* **2015**, *135*, 120−136.
(52) He, X.; Pang, S.; Ma, J.; Zhang, Y. Influence of relative humidity on heterogeneous reactions of O_3 and O_3/SO_2 with soot particles: Potential for environmental and health effects. *Atmos. Environ.* **2017**, *165*, 198−206.
(53) Shen, W.; Li, Z.; Liu, Y. Surface chemical functional groups modification of porous carbon. *Recent Pat. Chem. Eng.* **2008**, *1*, 27−40.
(54) Andrews, L. Resonance Raman spectrum of the matrix isolated ozonide ion in the species metal(+) ozonide(-). *J. Am. Chem. Soc.* **1973**, *95*, 4487−4488.
(55) Brodu, N.; Manero, M.-H.; Andriantsiferana, C.; Pic, J.-S.; Valdés, H. Role of Lewis acid sites of ZSM-5 zeolite on gaseous ozone abatement. *Chem. Eng. J.* **2013**, *231*, 281−286.
(56) Bulanin, K. M.; Lavalley, J. C.; Tsyganenko, A. A. Infrared study of ozone adsorption on CaO. *J. Phys. Chem. B* **1997**, *101*, 2917−2922.
(57) Wu, J.; Su, T.; Jiang, Y.; Xie, X.; Qin, Z.; Ji, H. In situ DRIFTS study of O_3 adsorption on CaO, γ-Al_2O_3, CuO, α-Fe_2O_3 and ZnO at room temperature for the catalytic ozonation of cinnamaldehyde. *Appl. Surf. Sci.* **2017**, *412*, 290−305.
(58) Roscoe, J. M.; Abbatt, J. P. D. Diffuse reflectance FTIR study of the interaction of alumina surfaces with ozone and water vapor. *J. Phys. Chem. A* **2005**, *109*, 9028−9034.
(59) Zhong, J.; Zeng, Y.; Chen, D.; Mo, S.; Zhang, M.; Fu, M.; Wu, J.; Su, Z.; Chen, P.; Ye, D. Toluene oxidation over Co^{3+}-rich spinel Co_3O_4: evaluation of chemical and by-product species identified by in situ DRIFTS combined with PTR-TOF-MS. *J. Hazard. Mater.* **2020**, *386*, 121957.
(60) Bulanin, K. M.; Lavalley, J. C.; Tsyganenko, A. A. Infrared study of ozone adsorption on TiO_2 (Anatase). *J. Phys. Chem.* **1995**, *99*, 10294−10298.
(61) Leba, A.; Davran-Candan, T.; Önsan, Z. I.; Yıldırım, R. DRIFTS study of selective CO oxidation over Au/γ-Al_2O_3 catalyst. *Catal. Commun.* **2012**, *29*, 6−10.
(62) Szanyi, J.; Kwak, J. H. Dissecting the steps of CO_2 reduction: 1. The interaction of CO and CO_2 with γ-Al_2O_3: an in situ FTIR study. *Phys. Chem. Chem. Phys.* **2014**, *16*, 15117−15125.
(63) Yao, S.; Weng, S.; Tang, Y.; Zhao, C.; Wu, Z.; Zhang, X.; Yamamoto, S.; Kodama, S. Characteristics of OH production by O_2/H_2O pulsed dielectric barrier discharge. *Vacuum* **2016**, *126*, 16−23.
(64) Song, Z.; Zhang, M.; Ma, C. Study on the oxidation of calcium sulfide using TGA and FTIR. *Fuel Process. Technol.* **2007**, *88*, 569−575.
(65) Courson, C.; Khalfi, A.; Mahzoul, H.; Hodjati, S.; Moral, N.; Kiennemann, A.; Gilot, P. Experimental study of the SO_2 removal over a NO_x trap catalyst. *Catal. Commun.* **2002**, *3*, 471−477.
(66) Kylhammar, L.; Carlsson, P.-A.; Skoglundh, M. Sulfur promoted low-temperature oxidation of methane over ceria supported platinum catalysts. *J. Catal.* **2011**, *284*, 50−59.
(67) Zhang, H.; Wen, X.; Wang, Y. Synthesis and characterization of sulfate and dodecylbenzenesulfonate intercalated zinc−iron layered double hydroxides by one-step coprecipitation route. *J. Solid State Chem.* **2007**, *180*, 1636−1647.
(68) Ryczkowski, J. IR spectroscopy in catalysis. *Catal. Today* **2001**, *68*, 263−381.
(69) Bannov, A. G.; Manakhov, A.; Shibaev, A. A.; Ukhina, A. V.; Polčák, J.; Maksimovskii, E. A. Synthesis dynamics of graphite oxide. *Thermochim. Acta* **2018**, *663*, 165−175.
(70) Li, J.-L.; Kudin, K. N.; McAllister, M. J.; Prud'homme, R. K.; Aksay, I. A.; Car, R. Oxygen-driven unzipping of graphitic materials. *Phys. Rev. Lett.* **2006**, *96*, 176101.
(71) Yao, S.; Mine, C.; Kodama, S.; Yamamoto, S.; Fujioka, Y. Experimental Investigation of Carbon Oxidization. *Chem. Lett.* **2009**, *38*, 168−169.
(72) Hug, S. J. In situ Fourier transform infrared measurements of sulfate adsorption on hematite in aqueous solutions. *J. Colloid Interface Sci.* **1997**, *188*, 415−422.
(73) Pietrogiacomi, D.; Sannino, D.; Magliano, A.; Ciambelli, P.; Tuti, S.; Indovina, V. The catalytic activity of $CuSO_4/ZrO_2$ for the selective catalytic reduction of NO_x with NH_3 in the presence of excess O_2. *Appl. Catal., B* **2002**, *36*, 217−230.
(74) Bulanin, K. M.; Lavalley, J. C.; Lamotte, J.; Mariey, L.; Tsyganenko, N. M.; Tsyganenko, A. A. Infrared study of ozone adsorption on CeO_2. *J. Phys. Chem. B* **1998**, *102*, 6809−6816.
(75) Wagner, C. D.; Taylor, J. A. Generation of XPS Auger lines by bremsstrahlung. *J. Electron Spectrosc. Relat. Phenom.* **1980**, *20*, 83−93.
(76) Boriboonsomsin, K.; Durbin, T.; Scora, G.; Johnson, K.; Sandez, D.; Vu, A.; Jiang, Y.; Burnette, A.; Yoon, S.; Collins, J.; Dai, Z.; Fulper, C.; Kishan, S.; Sabisch, M.; Jackson, D. Real-world exhaust temperature profiles of on-road heavy-duty diesel vehicles equipped with selective catalytic reduction. *Sci. Total Environ.* **2018**, *634*, 909−921.
(77) Jiang, B.; Zhao, S.; Wang, Y.; Wenren, Y.; Zhu, Z.; Harding, J.; Zhang, X.; Tu, X.; Zhang, X. Plasma-enhanced low temperature NH_3-SCR of NO_x over a Cu-Mn/SAPO-34 catalyst under oxygen-rich conditions. *Appl. Catal., B* **2021**, *286*, 119886.

https://doi.org/10.1021/acsomega.1c06659
ACS Omega 2022, 7, 8640−8650